Uniaxial negative thermal expansion and band renormalization in monolayer T_d-MoTe$_2$ at low temperature

Yu Ge,[1,2] Zhenyu Ding,[1,2] Wenjie Meng,[1] Jihao Wang ●,[1] Yubin Hou,[1] Gang Wu ●,[3,*]
Qingyou Lu,[1,4,5,6,†] and Xiaoping Yang ●[1,‡]

[1]*Anhui Province Key Laboratory of Condensed Matter Physics at Extreme Conditions, High Magnetic Field Laboratory,*
Chinese Academy of Sciences, Hefei 230031, China

[2]*Science Island Branch of Graduate School, University of Science and Technology of China, Hefei 230026, China*

[3]*Institute of High Performance Computing, 1 Fusionopolis Way, 16-16 Connexis, Singapore 138632, Singapore*

[4]*Hefei National Laboratory for Physical Sciences at the Microscale, University of Science and Technology of China, Hefei 230026, China*

[5]*Collaborative Innovation Center of Advanced Microstructures, Nanjing University, Nanjing 210093, China*

[6]*Hefei Science Center, Chinese Academy of Sciences, Hefei 230031, China*

The temperature-induced structure variation and its effect on physical properties is pivotal in material preparation for devices application. Motivated by surface scanning tunnel microscope (STM) measurement of T_d-MoTe$_2$ single crystal at low temperature, temperature dependent electronic structure, lattice dynamics, and topological properties are explored to understand the microscopic origin of the observed anisotropic negative thermal expansion and abnormal STM images below 70 K. Remarkably, we find that the nonequivalent Te atoms in T_d-MoTe$_2$ have qualitatively different contributions to both phonon spectra and electronic structures. The in-plane longitudinal acoustic mode and the Te$_{(2)}$ atoms are found to play an important role in uniaxial negative thermal expansion and the temperature dependent electronic phase transition, respectively. Interestingly, under the scalar relativistic approximation, a band renormalization occurs, accompanied by a Dirac phase transition from type II to type I, upon cooling below 70 K. Introducing spin-orbit coupling induces a temperature dependent semimetal–semiconductor transition. Our results explain the experimental phenomena very well: abnormal surface STM image below 70 K does not originate from the displacement of the Te atoms but the band renormalization owing to strong electron-lattice coupling.

I. INTRODUCTION

Layered transition metal dichalcogenides (TMDs) MX_2 (M = Mo, W; X = S, Se, Te) have attracted extensive research interest for both fundamental research and technical applications, due to their intriguing physical properties, including valley polarization effect [1–6], topological physics [7–19], superconductivity [20–26], etc. MoTe$_2$ is a representative two-dimensional (2D) TMD, since it is the only material that can be grown in three crystalline structures: hexagonal 2H phase [27], the distorted monoclinic $1T'$ phase [28], and orthorhombic T_d phase [26]; see Appendix A for details. Each phase has its unique electronic property. 2H-MoTe$_2$ is a typical semiconductor [29] and $1T'$-MoTe$_2$ is a semimetal [26]. When the temperature drops below 250 K, the monoclinic $1T'$ phase will convert to an orthorhombic T_d phase with the broken inversion symmetry [30] and superconductivity [26]. Theoretical calculations predicted that the T_d-MoTe$_2$ is a type-II Weyl semimetal [31], which is already confirmed experimentally [17]. In addition, MoTe$_2$ can make structural

phase transformation from the 2H phase to the $1T'$ phase by laser heating, and therefore has potential application in fabricating homojunction and phase change memories [32].

Recently, researchers discovered nonsaturating extremely large magnetoresistance in WTe$_2$ and MoTe$_2$ [33,34], and further "turn-on" phenomenon of magnetoresistance effect in the bulk T_d-MoTe$_2$ at low temperature [35]. In the process of studying the turn-on phenomenon in T_d-MoTe$_2$, Lu *et al.* found that the surface scanning tunnel microscope (STM) images show significant difference (see Appendix B) between 70 K and 7 K [35]. These indicate that surface MoTe$_2$ undergoes temperature-induced electronic phase transition at low temperature; meanwhile, a similar conclusion had been obtained based on the abnormal change of carrier density [36,37]. In sharp contrast to the intensive experimental studies, there is no theoretical investigation on this electronic phase transition due to the difficulty in determining the crystal structure and the corresponding electronic structures using *ab initio* simulations.

Significantly, surface STM experimental measurement observed that T_d-MoTe$_2$ exhibits anisotropic negative thermal expansion behavior with almost unchanged lattice constant a and drastically changing b at low temperature. When the temperature decreases from 70 K to 7 K, a changes from 6.33 Å to 6.37 Å, and the b changes from 3.47 Å to 3.61 Å [35]. An

intuitive reasoning is that there is direct relation between the possible electronic phase transition and the uniaxial negative thermal expansion.

The temperature-induced structure variation and its effect on physical properties is pivotal in material preparation for devices application. As a potential electronic material, the performance of $MoTe_2$-based devices can be altered significantly by the internal stress exerted by temperature dependent expansion at low temperature. Since the STM images investigate only the electronic density of the top layer T_d-$MoTe_2$ due to weak interlayer coupling, by extension, similar new physical phenomena should also exist in monolayer T_d-$MoTe_2$.

Herein, we focus on monolayer T_d-$MoTe_2$ and study the temperature dependent electronic structure, lattice dynamics, and topological properties by the first-principles method, aiming to explore the mechanism behind the experimentally observed novel phenomena. Remarkably, we find that the nonequivalent Te atoms in T_d-$MoTe_2$ have qualitatively different contributions to both phonon spectra and electronic structures, which is the origin of anisotropic negative thermal expansion and temperature dependent STM images. The in-plane longitudinal acoustic mode and the $Te_{(2)}$ atoms are found to play an important role in uniaxial negative thermal expansion and the temperature dependent electronic phase transition, respectively. Interestingly, under the scalar relativistic approximation, a band renormalization occurs, accompanied by a Dirac semimetal phase transition from type II to type I with the decreasing of temperature. Further introducing spin-orbit coupling lifts the spin degeneracy at the Dirac point due to inversion symmetry, and induces a temperature dependent semimetal–semiconductor transition. The considerable variation of energy bands around the Fermi level at the Γ point inevitably leads to highly different STM images at 70 K and 7 K.

II. THEORETICAL METHODS AND MODELS

The static lattice energy, the electronic band structure, and the Hellmann-Feynman force were calculated based on the plane-wave basis and projector augmented-wave method [38,39] as implemented in the Vienna *ab initio* simulation package (VASP)[40–43]. The exchange and correlation energy was considered in the generalized gradient approximation (GGA) level with a Perdew-Burke-Ernzerhof (PBE) functional [44]. The energy cutoff was set to 350 eV for a plane wave basis set. The tight-binding Hamiltonian was constructed by a projected Wannier functional method [45]. We used a periodic boundary condition and a vacuum layer of 25 Å that is thick enough to prohibit the out-of-plane electronic and dipole-dipole interactions between neighboring layers. The k-point interval in the first Brillouin zone (BZ) is 0.02 Å^{-1}. The atomic internal coordinates were optimized until the interatomic force is less than 10^{-6} eV/Å and total energy converges to 10^{-8} eV/unit cell. The phonon calculations were performed by using the supercell method [46]. The thermal expansion coefficient was calculated by using the SCF-QHA (self-consistent-quasiharmonic-approximation) method [47] based on the data obtained from first principle simulations.
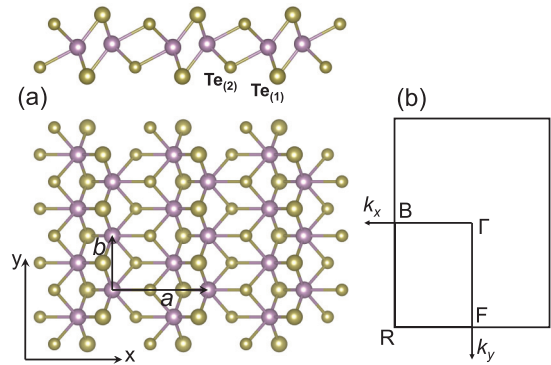

FIG. 1. (a) Schematic geometrical structures: side view (top panel) and top view (bottom panel) of the monolayer T_d-$MoTe_2$. (b) Two dimensional first Brillouin zone and high symmetry points.

III. RESULTS AND DISCUSSION

The geometrical structure of a monolayer T_d-$MoTe_2$ is shown in Fig. 1(a). The Mo atom is octahedral coordinated to the Te atoms. As the temperature decreases, the $MoTe_6$ octahedron deforms, and the Mo atom deviates the center of the Te octahedron along the x direction and forms a zigzag chain along the y direction. There are two nonequivalent Te atoms, and the bond lengths of Mo-$Te_{(1)}$ and Mo-$Te_{(2)}$ are 2.72 Å and 2.84 Å, respectively.

Surface STM measurements [35] show that the in-plane lattice constants a and b of the T_d-$MoTe_2$ is 6.33 and 3.47 Å at 70 K and 6.37 and 3.61 Å at 7 K. We take these experimental values as the in-plane lattice parameters of the monolayer T_d-$MoTe_2$. Although the STM images at 70 K and 7 K have significant differences [35], no experimental evidence indicates further phase transition below 100 K; therefore, the differences in STM images should be attributed to changes in the electronic structure around the Fermi level.

A. Lattice dynamics

Phonons play a crucial role in determining the thermodynamic properties of materials. Accurate phonon calculations are prerequisites for subsequent thermodynamic simulations. The monolayer T_d-$MoTe_2$ has six atoms in a unit cell, with a crystal structure of C_{2h} point group. In Fig. 2, we show the GGA phonon spectrum along the symmetry–lines Γ–F–R–B–Γ = (0, 0, 0)–(0, 0.5, 0)–(0.5, 0.5, 0)–(0.5, 0, 0)–(0, 0, 0) at 7 K. The blue and red shades represent the contributions of in-plane and out-of-plane vibrations of Mo/Te atoms to the phonon spectrum, respectively. The out-of-plane acoustic mode (ZA) is parabolic around the Γ point, which is a typical feature of the phonon spectrum of 2D materials. The ZA mode in 2D materials has considerable contribution for negative thermal expansion, while the in-plane longitudinal acoustic mode (LA) and the transverse acoustic mode (TA) show linear dispersion around the Γ point.

In general, the phonon spectrum is not sensitive to the temperature change from 70 K to 7 K. The high-frequency (>5 THz) and low-frequency (<5 THz) optical branches are mainly contributed by Mo atoms and Te atoms, respectively, which is similar to the situation of the monolayer 2H phase
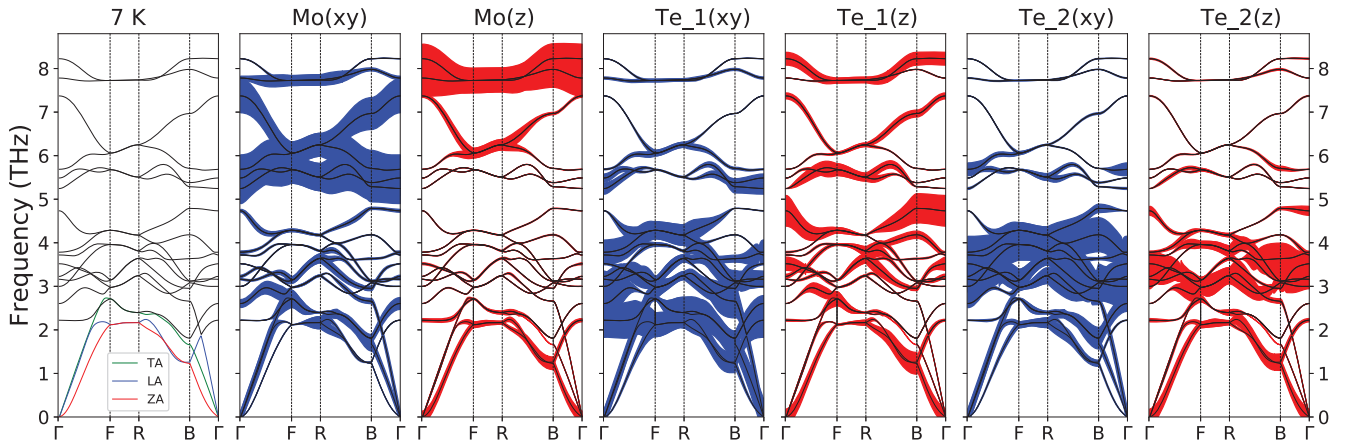
FIG. 2. Phonon dispersion diagram of the monolayer T_d-MoTe$_2$ at 7 K along the high symmetry paths. From left to right are the total phonon spectrum, the in-plane and out-of-plane contributions of Mo, Te$_{(1)}$, and Te$_{(2)}$ to the phonon spectrum, respectively.

[48,49]. However, compared to the Te$_{(2)}$ atom, the Te$_{(1)}$ atom has stronger hybridization with the Mo atom due to the shorter Mo-Te bond length. As a result, the spectrum of Te$_{(1)}$ atoms is relatively wider and overlaps partially with the acoustic branches, leading to the largest contribution to three acoustic modes, especially the TA mode along Γ–B. All of these indicate the lattice dynamic behaviors of the Te$_{(1)}$ and the Te$_{(2)}$ atoms are very different, which gives rise to different contributions to the macroscopic thermal expansion (shrinkage) of the system.

We calculate the Grüneisen parameter γ that describes the effect of changes in lattice volume on its vibrational properties, which represents the effect of temperature on lattice dynamics. To further understand the contributions of various modes to thermal expansion, the Grüneisen parameters for different vibration modes are plotted in Fig. 3. As can be seen from the figure, the Grüneisen parameters of the high-frequency optical branch vary between 0 and 2. The Grüneisen parameter of the ZA mode exhibits similar parabolic shape at both 7 K and 70 K, which is believed to be the main cause of the negative thermal expansion in common 2D material. Notably, the Grüneisen parameter of LA mode is also negative along Γ–F at 7 K and contributes to the negative thermal expansion, while it is positive at 70 K and offsets the effect of the ZA mode. Therefore, the negative thermal expansion
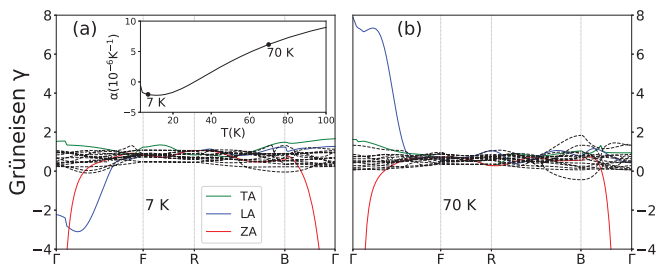

FIG. 3. Mode Grüneisen parameters of the monolayer T_d-MoTe$_2$ at 7 K (a) and 70 K (b). The green, blue, and red lines are Grüneisen parameters of TA, LA, and ZA mode, respectively. The inset of (a) is the evolution of the thermal expansion coefficient α with the change of temperature.

in T_d-MoTe$_2$ is different from the normal 2D materials. Due to the drastic temperature dependence of the Grüneisen parameter of the LA mode, the system undergoes a transition from positive thermal expansion to negative thermal expansion upon being cooled below 70 K. It is also worth noting that Grüneisen parameters of the LA mode are significantly different along the mutually orthogonal Γ–F and Γ–B, which reveals the anisotropic thermal expansion properties. In contrast, the thermal expansion of hexagonal 2H phase [48,49] is nearly isotropic. Surface STM experiment also confirmed the anisotropic negative thermal expansion effect, where the lattice constant b increases by 3.9% when the temperature is lowered from 70 K to 7 K; meanwhile, a changes only 0.6%.

Using the quasiharmonic approximation for atomic vibrations, the Grüneisen parameter γ can be related to the description of how the vibrational frequencies within a crystal are altered with changing volume. If the mode Grüneisen parameters are known for the wave vectors throughout the Brillouin zone, the temperature dependence of the Grüneisen constant and the linear thermal expansion coefficient α can easily be calculated [49,50]. The inset of Fig. 3(a) shows the thermal expansion coefficient α simulated by SCF-QHA with the change of temperature. The thermal expansion coefficient is negative from 0 to 32 K. The minimum value is -2.3×10^{-6} K^{-1} at 10 K. The thermal expansion coefficient turns out to be positive above 32 K, and the system begins to expand. These results are qualitatively consistent with those from the experimental STM measurements.

B. Electronic properties

We first calculate the GGA band structure without SOC of monolayer T_d-MoTe$_2$ along the symmetry lines Γ–F–R–B–Γ at 7 K and 70 K, as shown in Figs. 4(a) and 4(c). The system presents metallic behavior at both temperatures and, around the Fermi level, there is a symmetry-protected band crossing between two bands (labeled by red and blue in Fig. 4) belonging to different irreducible representations A and B along Γ–F line, which means that the crossing point is a strict quadruply degenerated Dirac point. We plot three-dimensional energy dispersion around the Dirac point
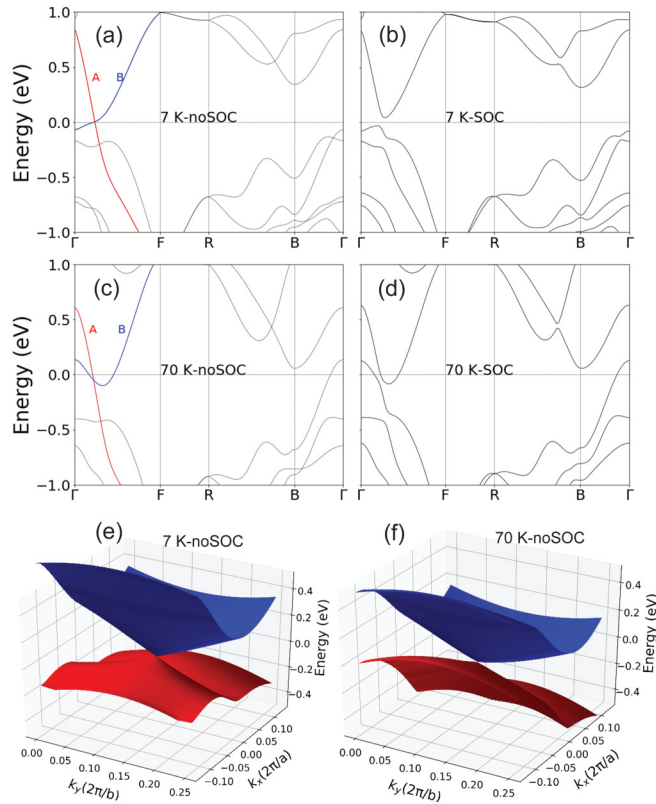
FIG. 4. GGA band structure of monolayer T_d-MoTe$_2$ without (a),(c) and with (b),(d) spin-orbit coupling at 7 K and 70 K, respectively. Three dimensional energy dispersion around the Dirac point at 7 K (e) and 70 K (f).
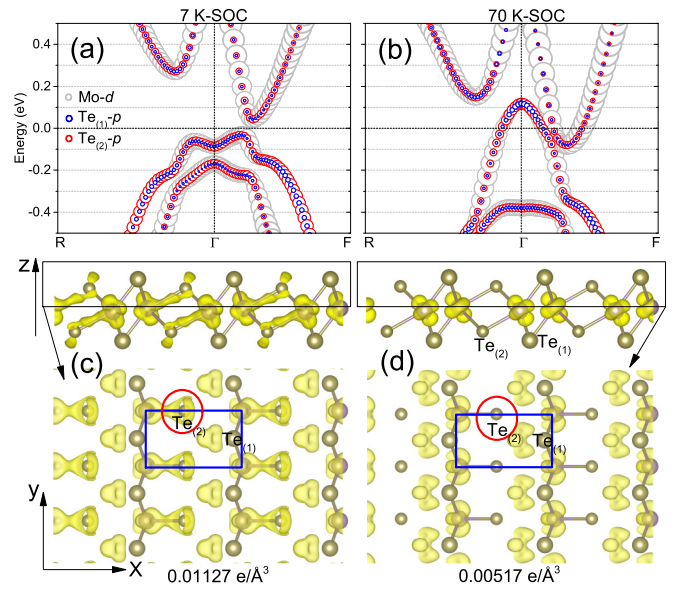

FIG. 5. GGA band structure with spin-orbit coupling at 7 K (a) and 70 K (b). The size of the symbol represents the contribution of the corresponding orbital. The partial charge density is calculated for the occupied states below valence band maximum at 7 K (c) or the Fermi level at 70 K (d) by 0.1 eV. The blue rectangle presents the 2D unit cell.

in Figs. 4(e) and 4(f), and the shape of the Dirac cone varies dramatically with the change of temperature, in line with the abrupt change of the blue band at the Γ point in energy by 0.2 eV [see Figs. 4(a) and 4(c)]. Therefore, in the absence of SOC, the monolayer T_d-MoTe$_2$ is a Dirac semimetal at 7 K and a metal with Dirac point around the Fermi level at 70 K. As the temperature decreases, the Dirac point shifts above the Fermi level, and the Dirac cone is significantly rotated out of plane, leading to a transformation from type II to type I, which is the origin of the abnormal surface STM image below 70 K. Due to the existence of inversion symmetry in monolayer T_d-MoTe$_2$, the introduction of SOC does not induce the emergence of the paired Weyl points, but instead a band inversion occurs and a small energy gap of 0.07 eV is turned on at 7 K, while the energy band at 70 K has a trivial semimetallic feature with the coexistence of electron and hole pockets. So, in the monolayer T$_d$-MoTe$_2$, the SOC effect causes a semimetal–semiconductor transition with the decreasing temperature.

Figures 5(a) and 5(b) show further the band dispersion with SOC along the symmetry-lines R–Γ–F of monolayer T_d-MoTe$_2$ in a 1 eV region around the Fermi level ($\varepsilon_F \equiv 0$). From the fatbands, we can conclude that the electronic properties of the system around ε_F are mainly controlled by the Mo-4d and Te$_{(2)}$-5p orbitals, and the proportion of Te$_{(1)}$-5p states is quite small, especially in the valence bands. Significantly, a band renormalization occurs around R–Γ–F

upon cooling below 70 K, with an order of 0.2 eV. Associated with it, the energy valley at Γ changes from hole type to electron type.

Experimentally it is observed that the surface STM image changes greatly from 70 K to 7 K (see Appendix B for details). In order to understand this phenomenon, we plot the partial charge density of the occupied states below valence band maximum at 7 K or the Fermi level at 70 K by 0.1 eV in Figs. 5(c) and 5(d), respectively. We can find that both Te$_{(1)}$-5p and Te$_{(2)}$-5p states should have no contribution to STM measurement at 70 K, but upon cooling to 7 K, an obvious charge density distribution located at Te$_{(2)}$ sites emerges. Therefore, our results explain the experimental observation perfectly. The abnormal surface STM image at 7 K does not originate from the displacement of the Te atoms but the band renormalization owing to strong electron-lattice coupling.

IV. CONCLUSIONS

In summary, our study on phonon spectrum and thermal expansion properties shows that the thermal expansion of monolayer T_d-MoTe$_2$ undergoes a transition from positive to negative with temperature decrease below 70 K, due to the drastic temperature dependence of the Grüneisen parameter of the LA mode. Along the mutually orthogonal Γ–F and Γ–B, the Grüneisen parameters of the LA mode are significantly different. As a result, the thermal expansion of the monolayer T_d phase presents an obvious uniaxial feature, which is consistent with the surface STM measurement. Under the scalar relativistic approximation, the monolayer T_d-MoTe$_2$ is a typical Dirac material. Upon cooling below 70 K, the band renormalization leads to a Dirac phase transition from type II to type I, which is the origin of an abnormal surface

STM image below 70 K. Due to the inversion symmetry in monolayer T_d-MoTe$_2$, introducing spin-orbit coupling does not produce paired Weyl points, but instead a band inversion occurs and a small energy gap of 0.07 eV is turned on at 7 K, while the energy band at 70 K has a trivial semimetallic feature with the coexistence of electron and hole pockets. As a result, the SOC effect causes a semimetal–semiconductor transition in the monolayer T_d-MoTe$_2$ with the decreasing temperature. Also, the intrinsic physical mechanism revealed in our work can be applied to other 2D TMD materials with the local MX_6 octahedron structure distortion.

APPENDIX A: THREE CRYSTALLINE STRUCTURES OF BULK MoTe$_2$
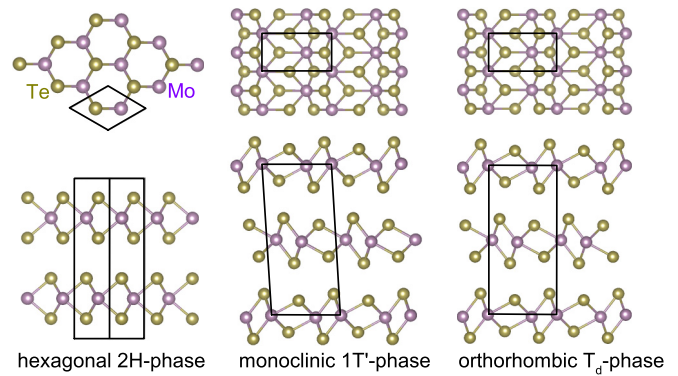
See Fig. 6 for schematic geometrical structures.

FIG. 6. Schematic geometrical structures: top views (top panels) and side views (bottom panels) of the three crystalline structures of bulk MoTe$_2$: hexagonal 2H phase, the distorted monoclinic $1T'$ phase, and orthorhombic T_d phase.

APPENDIX B: ABNORMAL SURFACE STM IMAGES AT 7 K AND 70 K

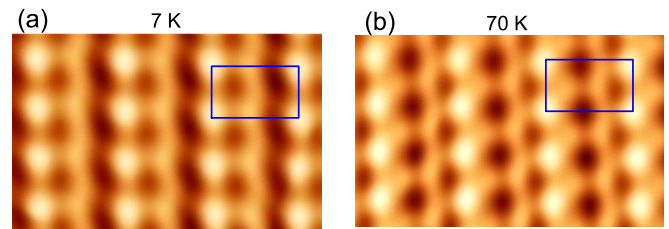See Fig. 7 for atomically resolved STM topographic images.

FIG. 7. Atomically resolved STM topographic image of the cleaved T_d-MoTe$_2$ surface at $T = 7$ K (a) and 70 K (b). The blue rectangle presents the 2D unit cell.

[1] D. Xiao, G. B. Liu, W. X. Feng, X. D. Xu, and W. Yao, Phys. Rev. Lett. **108**, 196802 (2012).

[2] H. L. Zeng, J. F. Dai, W. Yao, D. Xiao, and X. D. Cui, Nat. Nanotechnol. **7**, 490 (2012).

[3] K. F. Mak, K. He, J. Shan, and T. F. Heinz, Nat. Nanotechnol. **7**, 494 (2012).

[4] X. D. Xu, W. Yao, D. Xiao, and T. F. Heinz, Nat. Phys. **10**, 343 (2014).

[5] H. T. Yuan, M. S. Bahramy, K. Morimoto, S. F. Wu, K. Nomura, B. J. Yang, H. Shimotani, R. Suzuki, M. Toh, C. Kloc, X. D. Xu, R. Arita, N. Nagaosa, and Y. Iwasa, Nat. Phys. **9**, 563 (2013).

[6] D. MacNeill, C. Heikes, K. F. Mak, Z. Anderson, A. Kormanyos, V. Zolyomi, J. Park, and D. C. Ralph, Phys. Rev. Lett. **114**, 037401 (2015).

[7] X. F. Qian, J. W. Liu, L. Fu, and J. Li, Science **346**, 1344 (2014).

[8] Z. Y. Fei, T. Palomaki, S. F. Wu, W. J. Zhao, X. H. Cai, B. S. Sun, P. Nguyen, J. Finney, X. D. Xu, and D. H. Cobden, Nat. Phys. **13**, 677 (2017).

[9] L. Peng, Y. Yuan, G. Li, X. Yang, J. J. Xian, C. J. Yi, Y. G. Shi, and Y. S. Fu, Nat. Commun. **8**, 659 (2017).

[10] S. Tang, C. Zhang, D. Wong, Z. Pedramrazi, H.-Z. Tsai, C. Jia, B. Moritz, M. Claassen, H. Ryu, S. Kahn, J. Jiang, H. Yan, M. Hashimoto, D. Lu, R. G. Moore, C.-C. Hwang, C. Hwang, Z. Hussain, Y. Chen, M. M. Ugeda, Z. Liu, X. Xie, T. P. Devereaux, M. F. Crommie, S.-K. Mo, and Z.-X. Shen, Nat. Phys. **13**, 683 (2017).

[11] P. Chen, W. W. Pai, Y. H. Chan, W. L. Sun, C. Z. Xu, D. S. Lin, M. Y. Chou, A. V. Fedorov, and T. C. Chiang, Nat. Commun. **9**, 2003 (2018).

[12] S. F. Wu, V. Fatemi, Q. D. Gibson, K. Watanabe, T. Taniguchi, R. J. Cava, and P. Jarillo-Herrero, Science **359**, 76 (2018).

[13] A. A. Soluyanov, D. Gresch, Z. J. Wang, Q. S. Wu, M. Troyer, X. Dai, and B. A. Bernevig, Nature (London) **527**, 495 (2015).

[14] A. N. Berger, E. Andrade, A. Kerelsky, D. Edelberg, J. Li, Z. Wang, L. Zhang, J. Kim, N. Zaki, J. Avila, C. Chen, M. C. Asensio, S.-W. Cheong, B. A. Bernevig, and A. N. Pasupathy, npj Quantum Materials **3**, 2 (2018).

[15] J. Jiang, Z. K. Liu, Y. Sun, H. F. Yang, C. Rajamathi, Y. P. Qi, L. X. Yang, C. Chen, H. Peng, C. C. Hwang, S. Z. Sun,

S. K. Mo, I. Vobornik, J. Fujii, S. Parkin, C. Felser, B. Yan, and Y. Chen, Nat. Commun. **8**, 13973 (2017).

[16] K. Deng, G. L. Wan, P. Deng, K. N. Zhang, S. J. Ding, E. Y. Wang, M. Z. Yan, H. Q. Huang, H. Y. Zhang, Z. L. Xu, J. Denlinger, A. Fedorov, H. T. Yang, W. H. Duan, H. Yao, Y. Wu, S. S. Fan, H. J. Zhang, X. Chen, and S. Y. Zhou, Nat. Phys. **12**, 1105 (2016).

[17] L. Huang, T. McCormick, M. Ochi, Z. Y. Zhao, M. Suzuki, R. Arita, Y. Wu, D. X. Mou, H. Cao, J. Yan, N. Trivedi, and A. Kaminski, Nat. Mater. **15**, 1155 (2016).

[18] P. Li, Y. Wen, X. He, Q. Zhang, C. Xia, Z.-M. Yu, S. Y. A. Yang, Z. Y. Zhu, H. N. Alshareef, and X.-X. Zhang, Nat. Commun. **8**, 2150 (2017).

[19] I. Belopolski, D. S. Sanchez, Y. Ishida, X. C. Pan, P. Yu, S.-Y. Xu, G. Q. Chang, T.-R. Chang, H. Zheng, N. Alidoust, G. Bian, M. Neupane, S.-M. Huang, C.-C. Lee, Y. Song, H. J. Bu, G. H. Wang, S. S. Li, G. Eda, H.-T. Jeng, T. Kondo, H. Lin, Z. Liu, F. Q. Song, S. Shin, and M. Z. Hasan, Nat. Commun. **7**, 13643 (2016).

[20] B. Sipos, A. F. Kusmartseva, A. Akrap, H. Berger, L. Forro, and E. Tutis, Nat. Mater. **7**, 960 (2008).

[21] J. T. Ye, Y. J. Zhang, R. Akashi, M. S. Bahramy, R. Arita, and Y. Iwasa, Science **338**, 1193 (2012).

[22] T. Yokoya, T. Kiss, A. Chainani, S. Shin, M. Nohara, and H. Takagi, Science **294**, 2518 (2001).

[23] A. H. Castro Neto, Phys. Rev. Lett. **86**, 4382 (2001).

[24] Y. J. Yu, F. Y. Yang, X. F. Lu, Y. J. Yan, Y. H. Cho, L. G. Ma, X. H. Niu, S. Kim, Y. W. Son, D. L. Feng, S. Y. Li, S. W. Cheong, X. H. Chen, and Y. B. Zhang, Nat. Nanotechnol. **10**, 270 (2015).

[25] D. Costanzo, S. Jo, H. Berger, and A. F. Morpurgo, Nat. Nanotechnol. **11**, 339 (2016).

[26] Y. Qi, P. G. Naumov, M. N. Ali, C. R. Rajamathi, W. Schnelle, O. Barkalov, M. Hanfland, S. C. Wu, C. Shekhar, Yan Sun, V. Süß, M. Schmidt, U. Schwarz, E. Pippel, P. Werner, R. Hillebrand, T. Förster, E. Kampert, S. Parkin, R. J. Cava, C. Felser, B. Yan, and S. A. Medvedev, Nat. Commun. **7**, 11038 (2016).

[27] D. Puotinen and R. E. Newnham, Acta Crystallogr. **14**, 691 (1961).

[28] B. E. Brown, Acta Crystallogr. **20**, 268 (1966).

[29] T. Böker, R. Severin, A. Müller, C. Janowitz, R. Manzke, D. Voß, P. Krüger, A. Mazur, and J. Pollmann, Phys. Rev. B **64**, 235305 (2001).

[30] S. Cho, S. Kim, J. H. Kim, J. Zhao, J. Seok, D. H. Keum, J. Baik, D.-H. Choe, K. J. Chang, K. Suenaga, S. W. Kim, Y. H. Lee, and H. Yang, Science **349**, 625 (2015).

[31] Y. Sun, S.-C. Wu, M. N. Ali, C. Felser, and B. Yan, Phys. Rev. B **92**, 161107(R) (2015).

[32] Y. Wang, J. Xiao, H. Zhu, Y. Li, Y. Alsaid, K. Y. Fong, Y. Zhou, S. Wang, W. Shi, Y. Wang, A. Zettl, E. J. Reed, and X. Zhang, Nature (London) **550**, 487 (2017).

[33] M. N. Ali, J. Xiong, S. Flynn, J. Tao, Q. D. Gibson, L. M. Schoop, T. Liang, N. Haldolaarachchige, M. Hirschberger, N. P. Ong, and R. J. Cava, Nature (London) **514**, 205 (2014).

[34] F. C. Chen, H. Y. Lv, X. Luo, W. J. Lu, Q. L. Pei, G. T. Lin, Y. Y. Han, X. B. Zhu, W. H. Song, and Y. P. Sun, Phys. Rev. B **94**, 235154 (2016).

[35] Q. L. Pei, W. J. Meng, X. Luo, H. Y. Lv, F. C. Chen, W. J. Lu, Y. Y. Han, P. Tong, W. H. Song, Y. B. Hou, Q. Y. Lu, and Y. P. Sun, Phys. Rev. B **96**, 075132 (2017).

[36] Q. Zhou, D. Rhodes, Q. R. Zhang, S. Tang, R. Schönemann, and L. Balicas, Phys. Rev. B **94**, 121101(R) (2016).

[37] D. Rhodes, R. Schönemann, N. Aryel, Q. Zhou, Q. R. Zhang, E. Kampert, Y. C. Chiu, Y. Lai, Y. Shimura, G. T. McCandless, J. Y. Chan, D. W. Paley, J. Lee, A. D. Finke, J. P. C. Ruff, S. Das, E. Manousakis, and L. Balicas, Phys. Rev. B **96**, 165134 (2017).

[38] G. Kresse and D. Joubert, Phys. Rev. B **59**, 1758 (1999).

[39] P. E. Blöchl, Phys. Rev. B **50**, 17953 (1994).

[40] G. Kresse and J. Hafner, Phys. Rev. B **47**, 558 (1993).

[41] G. Kresse and J. Hafner, Phys. Rev. B **49**, 14251 (1994).

[42] G. Kresse and J. Furthmüller, Phys. Rev. B **54**, 11169 (1996).

[43] G. Kresse and J. Furthmüller, Comp. Mater. Sci. **6**, 15 (1996).

[44] J. P. Perdew, K. Burke, and M. Ernzerhof, Phys. Rev. Lett. **77**, 3865 (1996).

[45] A. A. Mostofi, J. R. Yates, Y.-S. Lee, I. Souza, D. Vanderbilt, and N. Marzari, Comput. Phys. Commun. **178**, 685 (2008).

[46] A. Togo and I. Tanaka, Scr. Mater. **108**, 1 (2015).

[47] L. F. Huang, X. Z. Lu, E. Tennessen, and J. M. Rondinelli, Comput. Mater. Sci. **120**, 84 (2016).

[48] L. F. Huang and Z. Zeng, J. Phys. Chem. C **119**, 18779 (2015).

[49] L. F. Huang, P. L. Gong, and Z. Zeng, Phys. Rev. B **90**, 045409 (2014).

[50] D. N. Talwar, M. Vandevyver, K. Kunc, and M. Zigone, Phys. Rev. B **24**, 741 (1981).

[51] https://www.nscc.sg